RSC Advances

ROYAL SOCIETY
OF **CHEMISTRY**

www.rsc.org/advances

ARTICLE TYPE

Surfactant CTAB-assisted synthesis of $Li_{1.13}[Ni_{0.233}Mn_{0.534}Co_{0.233}]_{0.87}O_2$ with festoon-like hierarchical architectures as cathode materials for Li-ion batteries with outstanding performance

Xianhua Hou[ab], Xiaoli Zou*[a], Yanling Huang[a], Shejun Hu*[ab], Qiang Ru[ab] and Yumei Gao[c]

5

Li-rich layered cathode materials $Li_{1.13}[Ni_{0.233}Mn_{0.534}Co_{0.233}]_{0.87}O_2$ are successfully synthesized by co-precipitation method with hexadecyl trimethyl ammonium bromide (CTAB) as surfactant. Structural and
10 electrochemical feature changes of resulted cathode materials have been studied thoroughly. When CTAB is considered as surfactant, a well-crystallized Li-rich layered cathode materials are obtained with Li_2CO_3 treatment for the festoon-like precursor hierarchically assembled by nanoplates. Among these oxides, the sample synthesized with CTAB shows a stable mixed phase on the edge of the powder particles and exhibits excellent electrochemical performance. The product delivers the highest initial discharge
15 capacity of 394 mAh g^{-1} at 0.1 C (1 C = 200 mA g^{-1}) between 2.5 and 4.8 V and 84.1% capacity is retained after 100 cycles. It is considered that the higher capacity and superior rate capability would be ascribed to the activation effect of CTAB, which can form a stable mixed structure and thus effectively alleviate the layered/spinel structure change during cycling.

.

20 ## Introduction

The introduction of non-aqueous rechargeable lithium-ion batteries in the 1990s for electric vehicles (EV), plug-in hybrid vehicles (PHEVs) and power portable electronic devices bring about a revolution in battery technology and a remarkable
25 transformation from the relatively low-voltage, low-capacity and water-based systems such as nickel-cadmium[1,2] and nickel-metal hydride batteries[3,4] because of their relatively high energy density and design flexibility. The electrochemical performances of the Li-ion batteries mainly depend on the cathode materials, the
30 anode materials and the electrolyte. While the anode materials have the characteristics of the specific capacity much higher than the cathode material, such as silicon-based[5-7], tin-based[8,9], Lithium transition metal oxides[10,11] and metal-oxides[12-14]. So it has become very important to improve the capability of cathode
35 material, and further to improve the capacity of lithium ion secondary batteries.

Owing to its easy preparation and stable electrochemical cycling performance, $LiCoO_2$ has been widely used in lithium ion batteries as positive electrode for almost two decades (the
40 theoretical capacity is 274 mAh g^{-1} and the practical capacity is 160 mAh g^{-1}).[15,16] However, the relatively high cost of cobalt have led to enormous efforts to look for new cathode materials that with superior capacity, energy density, safety and cycle life since 1991. To date, the olivine $LiFePO_4$ are considered to be

45 attractive due to iron as well as phosphate are abundant and thus low-priced raw materials, meanwhile it shows relatively high thermal stability and environmental harmlessness.[17,18] Nevertheless, low electronic/ionic conductivities and low energy density become the block in the practical application as compared
50 to $LiCoO_2$. Spinel $LiMn_2O_4$ is also proposed to be cathodes for Li-ion battery, due to its relatively high operation voltage (about 4.0 V) and superior rate performance. While this material has the disadvantages of poor cycle performance and low capacity (practical capacity is only about 120 mAh g^{-1}).[19,20] So the
55 electrochemical performance of conventional cathode materials, such as layered $LiCoO_2$, olivine $LiFePO_4$, and spinel $LiMn_2O_4$, cannot satisfactorily meet the demands for the extended driving range of lithium batteries.

Recently, Li-rich layered oxides with composite structures
60 $(xLi_2MnO_3·(1-x)LiMO_2, M = Ni, Co, Mn, etc.)$ have been extensively studied as promising cathode materials, providing much higher capacity than traditional cathode materials.[21-26] The high specific capacity of Li-rich layered cathode materials is ascribed to the reversible capacity from oxidation and reduction
65 of cations in the $LiMO_2$ component below 4.4 V and the irreversible capacity from electrochemical activation of the Li_2MnO_3 component above 4.4 V. As the Li_2MnO_3 component would transform into the electrochemically active MnO_2 by extracting Li_2O, the material can achieve an increased discharge
70 capacity over 280 mAh g^{-1} below 3 V when charged above 4.6

V.[27,28] And the resulting MnO_2 could not only participates the following charge/discharge process, but also function as a structural unit to stabilize the host $LiMO_2$ structure.

However, it is well-known that the extensive removal of Li ions leads to the large irreversible capacity and instability of the electrode structure which resulting in the structural transformation from the layered to spinel phase.[29] Hence, the Li-rich materials exist the disadvantages of voltage instability, capacity fading, slow charge/discharge rate and low powder tap density, which may be related to the structural change of these materials, such as the layered/spinel structure, cation mixing and phase unstability upon lithium extraction and insertion.[29,30] Some strategies have been proposed to overcome these issues.[31,32] The poor rate capability could be improved by surface modification of the cathode with nitridation, Sm_2O_3, Al_2O_3, Li-Mn-PO_4, graphene and CNT networks coating,[33-38] because the coating layers can effectively suppress SEI layer growth and maintain surface integrity by preventing transition metal dissolution. And low powder tap density could be improved by an optimized synthesis procedure via co-precipitation in flowing air using an oxide precursor.[39] Johnson et al. and Feng Wu et al. proposed that acid treatment and MoO_3 can greatly lower the first-cycle irreversible capacity.[40,41]

With the aim of achieving a high-performance of Li-rich materials, the $Li_{1.13}[Ni_{0.233}Mn_{0.534}Co_{0.233}]_{0.87}O_2$ cathode materials from $Ni_{0.233}Mn_{0.534}Co_{0.233}CO_3$ carbonate precursor by co-precipitation method were synthesized. In order to obtain uniform festoon-like spherical precursor particle, surfactant hexadecyl trimethyl ammonium bromide (CTAB) was introduced as a surfactant during the synthesis process. Surfactant can significantly reduce the surface tension and surface Gibbs free energy even in very low concentrations. By comparison with the high-performance of the material with CTAB as surfactant, the electrochemical properties of the resulted cathode materials with conventional complexant or oxidant are also studied, such as ammonia water and hydrogen peroxide which previous researchers proposed.[24, 42] The results show that the cathode materials with CTAB as surfactant has a stable mixed structure and thus possess superior electrochemical performance.

Experiment

Materials preparation

The Li-rich layered cathode material $Li_{1.13}[Ni_{0.233}Mn_{0.534}Co_{0.233}]_{0.87}O_2$ ($0.3Li_2MnO_3 \cdot 0.7Li[Mn_{1/3}Ni_{1/3}Co_{1/3}]O_2$) were all synthesized by co-precipitation method using different additive. While $MnSO_4 \cdot 4H_2O$, $NiSO_4 \cdot 6H_2O$ and $CoSO_4 \cdot 7H_2O$ (all are 99.9% in purity) were used as the raw transition metal hydrate. Sulphates of nickel, manganese and cobalt were dissolved in distilled water with stoichiometric ratio of 2.33 : 5.34 : 2.33 at a concentration of 1.5 M. And then 1.5 M Na_2CO_3 solutions were dropped slowly to the well-prepared solution in continuous stirred tank reactor (CSTR) to form the uniformly co-precipitated carbonate of Mn, Ni and Co. Meanwhile the different additive, a desired amount of ammonium hydroxide ($NH_3 \cdot H_2O$, 25 wt%), hydrogen peroxide (H_2O_2) or hexadecyl trimethyl ammonium bromide (CTAB), was added into the mixed solution respectively. The pH value in the

reactors was maintained at about 8.0, while the reaction temperature was keep at approximately 60 ℃. After stirring for 4 h, the obtained suspension solution was filtered and washed by distilled water for few times and then the precipitation was dried at 80 ℃ over night. When the precursor was dried, a stoichiometric amount 5% excess of lithium carbonate was mixed thoroughly with the dried powder and then initially heated to 480 ℃ and subsequently calcined at 850 ℃ for 24 h to obtain $Li_{1.13}[Ni_{0.233}Mn_{0.534}Co_{0.233}]_{0.87}O_2$ powders (marked LNMCO-NH, LNMCO-HO, LNMCO-CTAB respectively hereafter). In order to compare with above samples, one contrastive sample was produced, similar procedure was made except none additive was added into the CSTR when precursors was synthesized (marked LNMCO-HO hereafter).

Structural characterization

The phase analysis of the different samples were performed using X-ray diffraction (XRD; PANalytical X'Pert PRO, Cu/Kα radiation, λ = 0.15406 nm) with Cu Kα radiation in a 2θ range from 10° to 90° at a scan rate of 5° min^{-1}. The morphology and structure of the $Li_{1.13}[Ni_{0.233}Mn_{0.534}Co_{0.233}]_{0.87}O_2$ compound was examined by a scanning electron microscope (SEM; ZEISS ULTRA 55) and transmission electron microscopy (TEM; JEM-2100HR), accompanying with the selected area electron diffraction (SAED). Raman spectra were obtained with HR800UV Raman microspectrometer (Jobin Yvon; France) with a 514.53 nm argon laser as the excitation source.

Electrochemical evaluation

Electrochemical measurements were carried out using CR2430 coin-type cells. The positive electrodes for the electrochemical studies were prepared by coating a mixture containing 80% active materials, 10% acetylene black and 10% polyvinylidene fluoride (PVDF) binder, which dissolved in n-methyl-2-pyrrolidone solvent, on circular Al current collector foils. Then the electrode was dried at 120 ℃ for overnight in vacuum and punched into 18 mm diameter disks. The electrode CR2430 coin-type cells were assembled in an argon-glove box with organic was 1 M LiPF6 dissolved in a mixture of ethylene carbonate (EC), ethylmethyl carbonate (EMC) and diethyl carbonate (DEC) at a volume ratio of 1 : 1 : 1 as electrolyte (provided by Chei Industries Inc., South Korea). Lithium metal was used as the counter and reference electrodes, while Celgard-2400 as the separator. Charge and discharge tests were all performed galvanostatically at current density of 20 mA g^{-1} between 2.5 and 4.65 V versus Li/Li^{+}. The rate capability was measured by varying the discharge current density at 20, 40, 100, 200, 400, 600, 800 and 1000 mA g^{-1} (0.1C, 0.2C, 0.5C, 1C, 2C, 3C, 4C, 5C). All the charge and discharge measurements were performed by a Xin Wei BT-2043 battery testing system at 25 ℃. Cyclic voltammograms (CVs) were measured in Solartron 1470E electrochemistry system at a scanning rate of 0.1 mV s^{-1}. In additional, electrochemical impedance spectrum (EIS) was also performed under a frequency range 100 kHz - 0.01 Hz using a vibration voltage of 5 mV to determine the resistance of the cycled cells.

Results and discussion

XRD and Raman are studied to investigate the phase structures of

the samples. Fig. 1a compares the XRD patterns of the synthesized $Li_{1.13}[Ni_{0.233}Mn_{0.534}Co_{0.233}]_{0.87}O_2$ with different additive. Fig. 1a shows that all the sintered composites present well-defined layer structure based on the hexagonal a-NaFeO$_2$

5 structure with R3m space group and no impurity phases, except for some weak peaks between 20° to 25°. The weak peaks between 20° and 25° are supposed to be attributed to the superlattice ordering of Li and Mn in the transition-metal layers of Li_2MnO_3 which corresponding to the C/2m structure.[26] And

10 the obvious split peak of the (108) and (110) observed for all samples indicates a well layered structure.
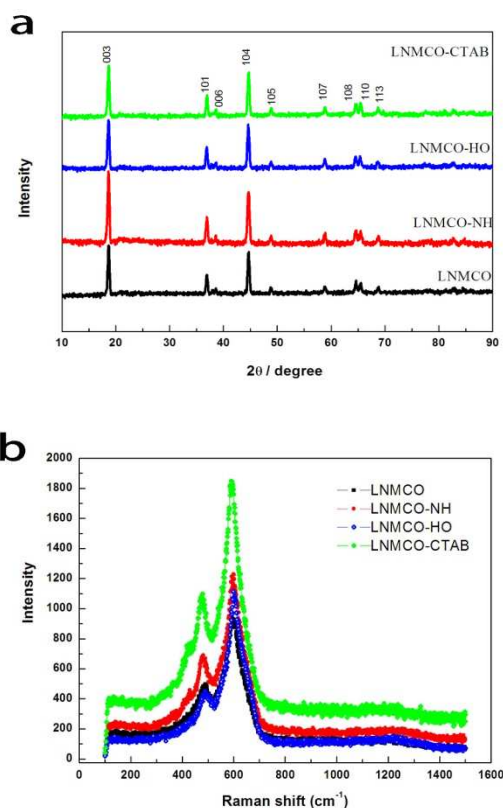
Fig. 1 XRD patterns (a) and Raman spectra (b) of the synthesized
15 $Li_{1.13}[Ni_{0.233}Mn_{0.534}Co_{0.233}]_{0.87}O_2.$

The Raman spectra collected from the products in the region of 100-1500 cm^{-1} are shown in Fig. 1b. A high-frequency peak in the spectral range 580-600 cm^{-1} and a low-frequency in the spectral range of 490-510 cm^{-1} are observed. These data clearly

20 evidence the Raman-active Eg and A$_1$g modes for the layered $LiMO_2$ in the D$_5$3h spectroscopic symmetry.[43] Meanwhile, an obscure peak appears at 415 cm^{-1}, which corresponds to the explicit presence of the Li_2MnO_3 in the structure.[44] The observed results from XRD pattern and Raman spectra illustrate that all the

25 samples are composed of layered Li_2MnO_3 and $LiMO_2$ structure.

Differences among the morphologies and particle sizes of the four samples of precursors and $Li_{1.13}[Ni_{0.233}Mn_{0.534}Co_{0.233}]_{0.87}O_2$ cathode materials are evident, as shown in Fig. 2. From the low-magnification SEM images (the insert one), we can see that all

30 the precursor samples present uniform micro-sphere morphology except for the sample LNMCO-NH that presents a few submicro-
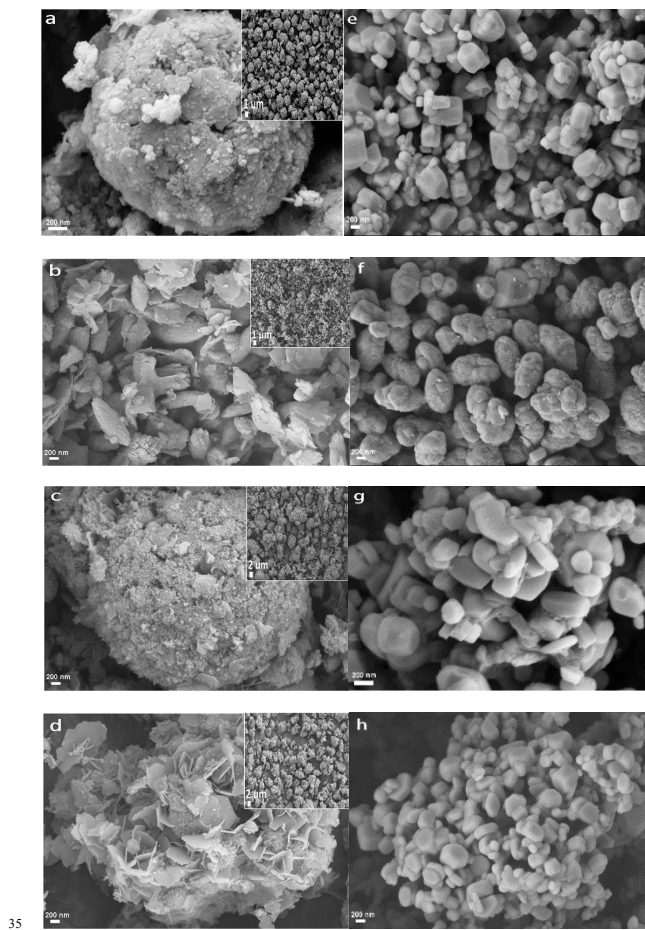
35 **Fig. 2** High-magnification and low magnification (insert) SEM image of the precursor MCO$_3$ and the $Li_{1.13}[Ni_{0.233}Mn_{0.534}Co_{0.233}]_{0.87}O_2$ composites. (a-d) the precursors LNMCO, LNMCO-NH, LNMCO-HO, LNMCO-CTAB and (e-h) the corresponding $Li_{1.13}[Ni_{0.233}Mn_{0.534}Co_{0.233}]_{0.87}O_2$
40 composites.

ellipse structure and a large quantity of flake structure coexisted. Further, the high-magnification SEM observations show that all the precursor products aggregated by a great deal of nanoplates or nanoparticles. Fig. 2a reveals that the cabbage-like micro-sphere,

45 which the diameter is about 2.3 um, was structured by the nanoplates accumulation layer upon layer with thickness of ~40 nm. When adding ammonium hydroxide into the raw materials, the nanoplates (Fig. 2b) start to disperse completely and recombined to smaller submicro-ellipse partialy with diameter of

50 440 nm-1um. Meanwhile the thickness of the nanoplates deduce to ~28 nm. As the additive change to the oxidant H$_2$O$_2$, the surface of microsphere are coated by a mass of nanoparticles lead to the enlargement of microsphere's diameter of ~5 um as seen from the Fig. 2c. Fig. 2d indicates that the nanoplates with the

55 thickness of ~15 nm are arranged vertically and connected with each other to form the unusual hierarchical festoon-like morphology when CTAB introduced. However, the lithiation process for all the precursors causes a remarkable morphological variation to nanocrystals.

60 Fig. 2e-h present that all the as-synthesized lithiated products are composed of nanocrystal expect for LNMCO-NH sample that reunited to submicro-ellipse structure. What can be explain the

ARTICLE TYPE
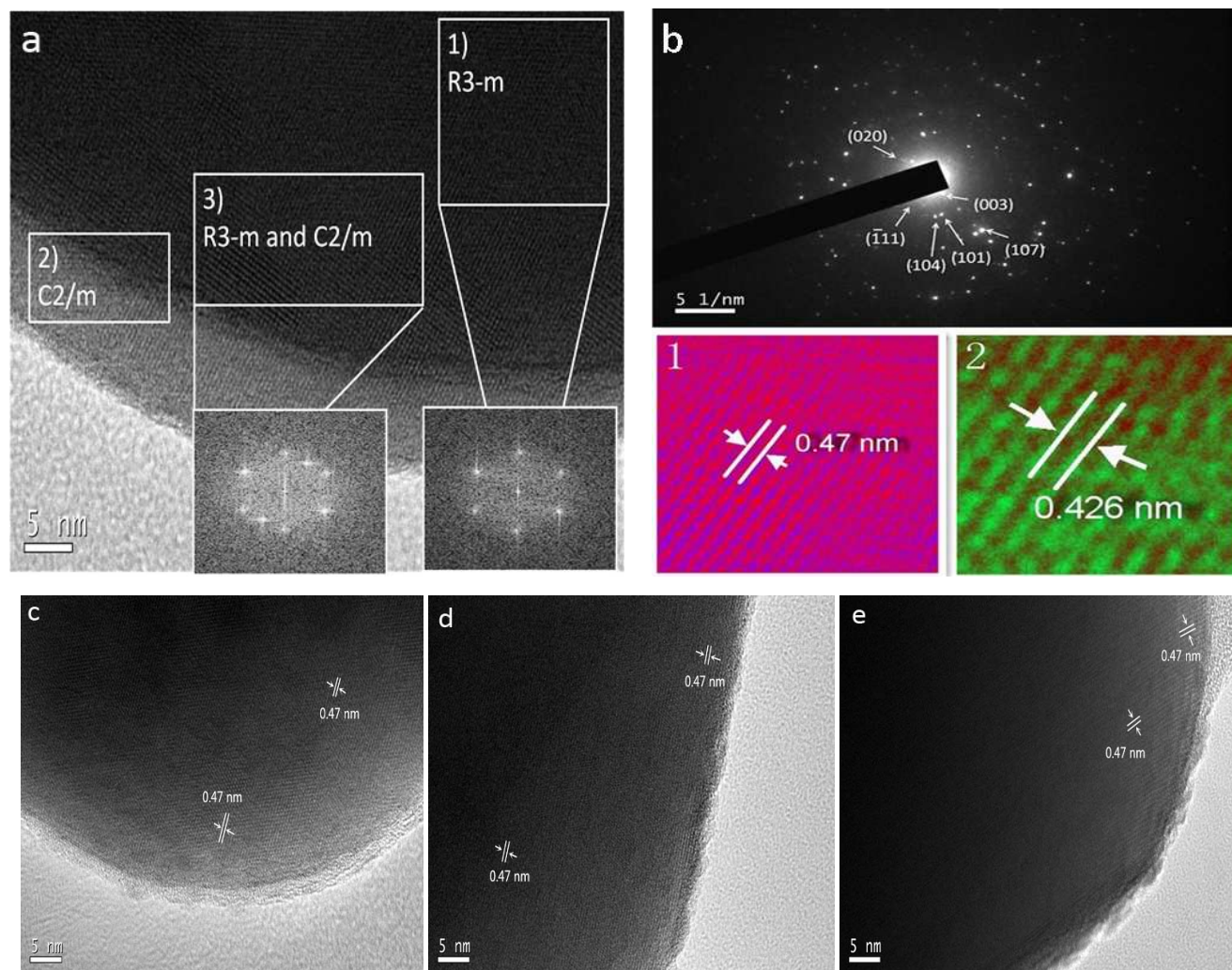
₅ **Fig. 3** (a) TEM image of LNMCO-CTAB and the insert are the corresponding FFT pattern of the selected region, (b) the color lattice image of the 1 or 2 region and the corresponding SAED of the particles, (c)-(e) the TEM image of LNMCO, LNMCO-NH and LNMCO-OH respectively.

different evolution of precursor morphology upon lithiation is the rearrangements of transition metal, lithium and oxide element to ₁₀ layered $Li_{1.13}[Ni_{0.233}Mn_{0.534}Co_{0.233}]_{0.87}O_2$ structure during the high-temperature calcination at 850 ℃ . [45] The as-prepared lithiated oxide LNMCO-CTAB (Fig. 2h) appear polyhedron morphology, dispersion characteristics, smooth surfaces, small size and narrow particle size distribution that gives a high surface ₁₅ area, short distance of lithium ion transport and greatly influences the electrochemical properties such as rate capability and discharge capacity. The cationic surfactant CTAB plays the role of prompting the combination between the metal cation and carbonate ions to develop uniformly spherical precursor particles

₂₀ weaved by the nano-sheet, which can react with lithium carbonate fully to form better crystallinity, smaller particle of final product in the process of heat treatment.

In order to find out how the crystalline structure works as an ₂₅ important role in determination of the electrochemical performance for the LNMCO-CTAB, the transmission electron microscope (TEM) technology is carried out. The corresponding fast Fourier transform (FFT) images and color lattice image are also given in Fig 3. As shown in Fig 3a, two structures within ₃₀ LNMCO-CTAB could be found: the R-3m layered rhombohedral structure and the C2/m layered monoclinic structure. As seen from the magnified color IFFT images on periphery and inner

part of a single particle (Fig 3a), the inner part of the grain have a regular lattice finger print of d = 0.47 nm corresponding to the (003) plane of rhombohedral $LiCoO_2$.[32] A clear lattice fringe appears at the periphery of the particle (the thickness is around 8 nm) corresponding to the typical C2/m layered materials with (020) plane (d = 0.426 nm) of monoclinic Li_2MnO_3. The mixed region (the "3" region) FFT shows that composite character of the product is structurally integrated with the two above structures (R-3m and C2/m). Moreover, it is clear that the product is composed of rhombohedral $LiCoO_2$-like and monoclinic Li_2MnO_3-like structure from the SAED pattern (Fig. 3b), which the lattice plane (003), (104), (101), (107) belongs to rhombohedral structure and ($\bar{1}11$), (020) are ascribed to monoclinic structure.[34] Therefore from the lattice image of CTAB-added sample, three phases can be observed from the edge to the inner part of the particle. They are C2/m phase, mixed phase and R3-m phase respectively. While from the TEM images of LNMCO, LNMCO-NH and LNMCO-OH samples, only one phase corresponding to (003) plane of rhombohedral $LiCoO_2$ is found in Fig. 3c-e.

Because the lattice image of TEM results just response the major crystal plane or overlap major planes from the Li_2MnO_3/$Li[Mn_{1/3}Ni_{1/3}Co_{1/3}]O_2$. So the only one lattice plane observed from the TEM image may be owing to the whole combination of major crystal plane of Li_2MnO_3 and $Li[Mn_{1/3}Ni_{1/3}Co_{1/3}]O_2$ in every parts of the particles. While from the lattice image of

CTAB-assisted sample, three phases can be observed from the edge to the inner part of the particle. It means the CTAB-assisted sample presents the peculiar combination of the two phases and this special structure can effectively alleviates the structure change in the cycling process. In addition, these TEM observations all also agree well with previous XRD and Raman results.

Fig. 4 shows the charge/discharge profiles and CV curves of different $Li_{1.13}[Ni_{0.233}Mn_{0.534}Co_{0.233}]_{0.87}O_2$ samples between 2.5 and 4.65 V after the 1st, 2nd cycle in coin-type lithium cells at 25 °C. As normal Li-rich layered oxides, shown in Fig. 4a, there is a charge platform above 4.4 V which appears only in the initial cycle and an unconspicuous one below 4.4 V which ascribed to the reaction of lithium taking off or embedding from LMO_2.[46,47] As shown in figures, each samples display the typical smooth shape of the initial discharge and subsequent charge/discharge curves without any obvious plateaus. Among these samples, LNMCO-CTAB has the largest initial charge and discharge capacity of 402 mAh g^{-1} and 290 mAh g^{-1}. By using the same C-rate (0.1C), the initial discharge capacities of other samples are 248, 171 and 222 mAh g^{-1} for LNMCO, LNMCO-NH, LNMCO-HO respectively. While the initial columbic efficiency of LNMCO-CTAB is about 72.3% against 71%, 68%, 69.8% for the LNMCO, LNMCO-NH, LNMCO-HO samples respectively. The high irreversible capacity loss of the LMNCO may be attributed to widespread decomposition of electrolyte on the particle surface
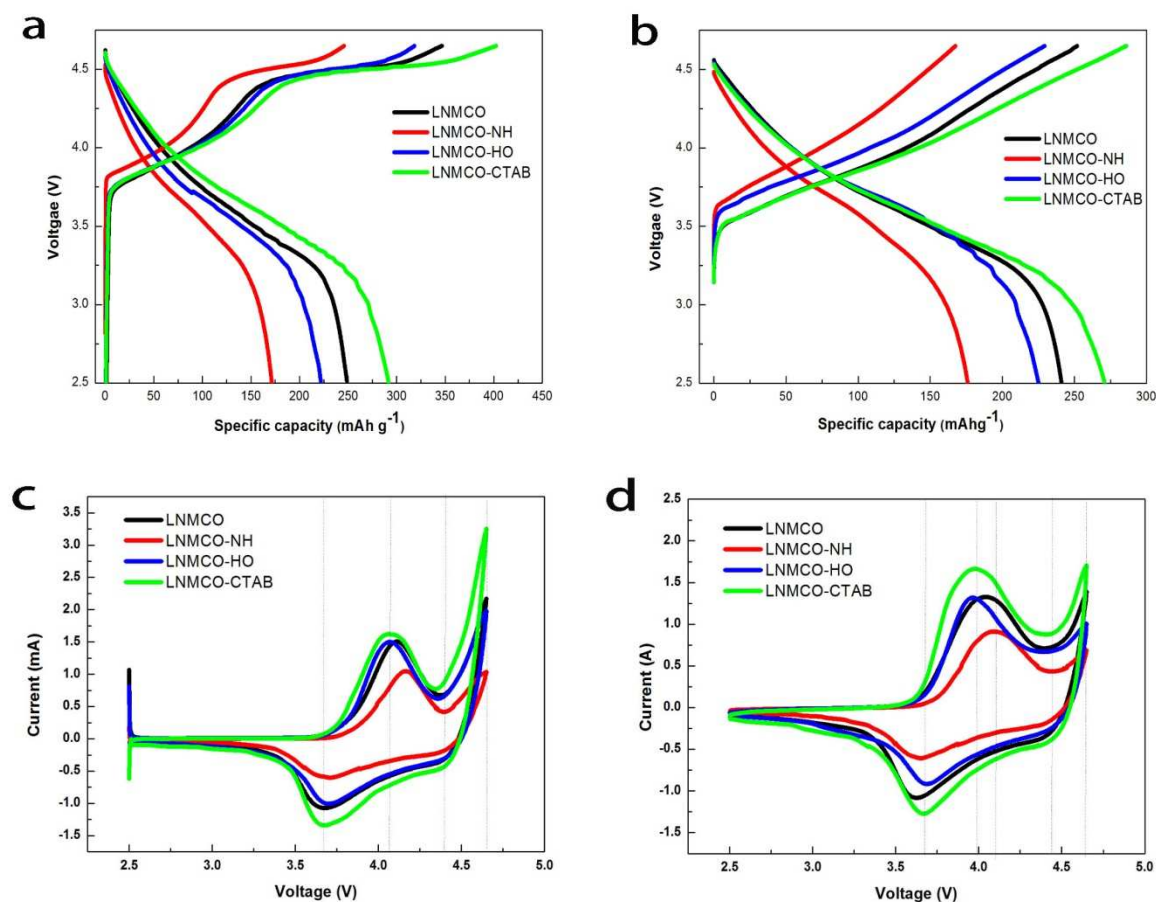
Fig. 4 Charge/discharge curves at 0.1 C rate of $Li_{1.13}[Ni_{0.233}Mn_{0.534}Co_{0.233}]_{0.87}O_2$ synthesized with different additive (a) in the initial cycle, (b) in the second cycle and CV curves (c) in the initial cycle, (d) in the second cycle

ARTICLE TYPE

to form SEI film and irreversible oxygen loss with Li ion (Li_2O) in Li_2MnO_3 to form active MnO_2 component. This SEI film hinders the direct contact between Li-ion and electrode–electrolyte interface and thus reduces the specific capacity of the 5 positive electrode. As shown in Fig. 4a and 4b, there are no obvious platform at the second charge/discharge curves any more, meanwhile the specific capacity of sample LNMCO-CTAB is greater than other samples.

Cyclic voltammetry (CV) analysis is conducted to evaluate the 10 redox potential of the transition metal ions during cycling. As can be seen from Fig. 4c, for all the samples, there is two main oxidation peaks, one anodic peak at about 4.0-4.4 V and another at about 4.6-4.7 V in the initial charge. The peak at low potential ascribed to the extraction of Li ion from the $LiMO_2$ (M = Mn, Ni, 15 Co) structure, is associated with oxidation from Ni^{2+} to Ni^{4+} and oxidation from Co^{3+} to Co^{4+}.[48] And another higher potential peak at 4.6-4.7 V is related to the extraction of Li_2O from Li_2MnO_3 to form active MnO_2 component,[27] which is an irreversible electrochemical activation reaction. During the first discharge 20 process, there are also two reduction peaks at about 4.3-4.5 V and 3.5- 3.7 V which are the corresponding cathode peaks of Co^{4+} to Co^{3+} and Ni^{4+} to Ni^{2+}. It can be found that the peaks at 4.6-4.7 V decrease markedly (Fig. 4d), while a new reduction peak appears at 3.0-3.3 V for all the samples in the following cycles. The new 25 peaks can be associated to the reduction of Mn^{4+} triggered by the electrochemical activation of Li_2MnO_3 in the first charge process. Owing to the removal of Li_2O is an irreversible process, the initial discharge capacity is much lower than first charge capacity (Fig. 4a). Interestingly, the oxidation peaks at 4.0-4.4 V for all 30 samples are all shift to lower voltage which may be the migration of Ni element migration during the lithium extraction/insertion process.[29] However all the peaks intensity of sample LNMCO-CTAB is stronger than other samples. That means there may be more Co ion and Ni ion participating the electrochemical reaction 35 in sample LNMCO-CTAB than other samples and less cation mixture during cycling ensuring high capacity and coulombic efficiency.

The cycling performance at 0.1 C is present in Fig 5a. As one can see that at the completion of 100th cycles, a high discharge 40 capacity of 247.5 mAh g^{-1} is maintained for sample LNMCO-CTAB, while sample LNMCO-NH suffers from the lowest capacity of 158 mAh g^{-1} after 100 cycles inferring from Fig. 5a. The results also reveal good cycling performance of sample LNMCO-CTAB with high capacity retention ratio of 84.1%. As 45 the large particle sizes of LNMCO-NH may be partly leads to the poor electrochemical performance due to the small specific surface area and long Li-ion diffusion distance,[49] the sample LNMCO-NH shows the lowest capacity and initial efficiency. Furthermore, this improvement of LNMCO-CTAB in the 50 electrochemical features may mainly due to the presence of the stable mixed structure, smaller particle size and depressed side reactions between electrolyte and charged cathode materials. This results can be supposed that the mixed structure is very effective

to block the side reactions with the electrolytes and alleviate the 55 structure change from layered to spinel during the cycle ensuring high capacity and cycle performance.
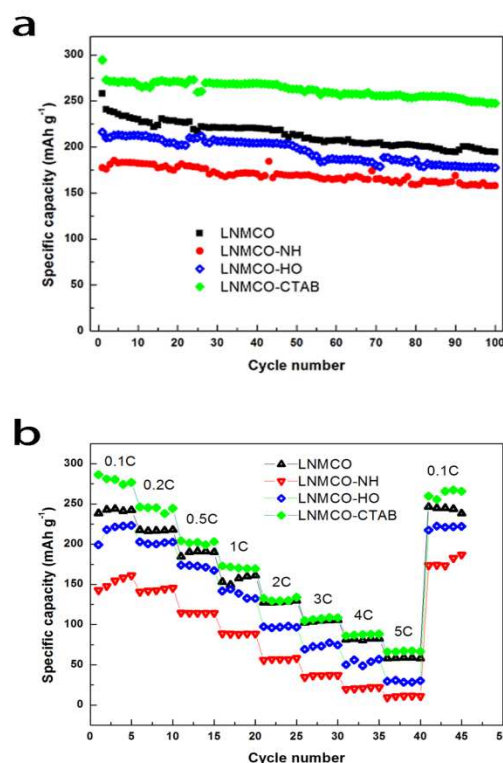
Fig. 5 (a) Cycling performance at 0.1C and (b) rate capabilities at various 60 C rates of the $Li_{1.13}[Ni_{0.233}Mn_{0.534}Co_{0.233}]_{0.87}O_2$ half-cells.

For rate performance comparison, the discharge capacity of all samples at various C-rate is presented in Fig. 5b. In this test, the cell was charged/discharged for 5 cycles with current density of 20 mA g^{-1} (0.1C-rate) and then performed five cycles at each 65 increasing C-rate from 0.2 to 5C. With the applied current density increasing, all the samples present gradual decreases of discharge capacity. The discharge capacity of sample LNMCO-CTAB dropped to 66.7 mAh g^{-1} by applying a higher current density of 1000 mA g^{-1} (5C-rate), but clearly, it exhibit highest discharge 70 capacities at all rates, while the corresponding capacity of sample LNMCO-NH is only 11.1 mAh g^{-1} at 5C-rate. In addition, it is worth mentioning that the discharge capacity of the outstanding sample is recovered with a better efficiency of 96.1% when the current density back to 20 mA g^{-1} from 1000 mA g^{-1}. Thus it can 75 be seen that the sample LNMCO-CTAB possess higher capacity as well as better rate capability. This suggests that the mixed structure on the edge was stable for intercalation of Li ion at the high and low rechargeable rate. Such a significant improvement is also attributed to the uniform and smaller particle size which 80 can shorten the Li ion diffusion path effectively.[50]

Electrochemical impedance spectroscopy has been performed to understand the difference in electrochemical performance for $Li_{1.13}[Ni_{0.233}Mn_{0.534}Co_{0.233}]_{0.87}O_2$ electrodes prepared with different additives. The measured impedance spectra are presented in Fig. 6a and b and the insert is the equivalent circuit corresponding to the EIS spectra. The shapes of the Nyquist plots are similar. They are all composed of a semicircle in the high frequency and a semicircle in the high to medium frequency. As is know, the semicircle at high frequency can be ascribed to the formation of solid electrolyte interface (SEI) film and contact resistance (R_{SEI}), while the one at mid-frequency is attributed to charge/discharge resistance at the interface of electrode and electrolyte (R_{ct}).[24,27] The inclined straight line in the low frequency which is assigned to the Warburg impedance due to the concentration polarization of the electrode even disappears

because of the large R_{ct}. Meanwhile, the fitting results of R_{SEI} and R_{ct} are listed in Table 1. As indicated, the R_{SEI} value is relatively small as compared to R_{ct} value during cycling. Such phenomenon can be ascribed to the side reaction takes place between active electrode and the electrolyte, the poor conductivity of Li_2MnO_3 and structure change due to the extensive removal of Li_2O from Li_2MnO_3 during the cycling.[28] This effect would make the cell impedance increase and the capacity decline during cycling, especially at high current rates. It also reveals distinctly that the R_{ct} of LNMCO-CTAB is smaller than that of other samples both at the 1st cycle and 100th cycle. Furthermore, it is worth pointing out that the variation of the R_{SEI} and R_{ct} are not distinct compared to the other samples during the cycles and the R_{ct} maintain at 1200-1500 Ω. Therefore, the stable structure is supposed during the cycle, which can owe to the stable mixed structure on the edge of particles. Because the electrochemical performance is mainly influenced by the charge transfer resistance, so the sample LNMCO-CTAB possess superior electrochemical performance from the analysis at the Fig. 5.[22]

Conclusion

In summary, lithium-rich layered oxide $Li_{1.13}[Ni_{0.233}Mn_{0.534}Co_{0.233}]_{0.87}O_2$ with different additives have been investigated. As a result, morphological changes occurred when the different additives were added in the synthesis process. After a desired amount of CTAB was introduced as surfactant, the precursor presented a hierarchical festoon-like architectures and a stable mixed structure has been detected for $Li_{1.13}[Ni_{0.233}Mn_{0.534}Co_{0.233}]_{0.87}O_2$ from TEM morphology. During the initial charge process, the initial coulombic efficiency of the cell has been increased to 72.3% from 69.5% and the capacity retention is elevated to 72.3% after 100 cycles (the specific capacity maintain at 247.5 mAh g^{-1}). On account of the smaller particle size and stable mixed structure on the edge of particle, the material LNMCO-CTAB delivers higher discharge capacity at various charge rates. Furthermore, the material LNMCO-CTAB showed the lowest and stable R_{ct} values during cycling because of the stable mixed structure. This paper suggests that the Li-rich layered cathode materials synthesized with CTAB as surfactant can construct a stable mixed structure and then exhibit a good cycle performance.

Fig. 6 Nyquist plots of EIS spectra for the synthesized $Li_{1.13}[Ni_{0.233}Mn_{0.534}Co_{0.233}]_{0.87}O_2$ after 1st cycle (a) and 100th cycle (b) at 0.1 C

Table 1 The AC impedance values of R_{SEI} and R_{ct} after 1st cycle and 100th cycle.

		LNMCO	LNMCO-NH	LNMCO-HO	LNMCO-CTAB
1st	$R_{SEI}(\Omega)$	310.20	210.8	280.47	260.56
	$R_{ct}(\Omega)$	1250.35	4214.6	4610.6	1206.46
100th	$R_{SEI}(\Omega)$	215.36	215.65	135.8	274.53
	$R_{ct}(\Omega)$	4620.55	2950.58	3350.41	1512.35

Notes

RSC Advances Accepted Manuscript

a Laboratory of Quantum Engineering and Quantum Materials, School of Physics and Telecommunication Engineering, South China Normal University, Guangzhou 510006, China, Tel: +86 20 39310066
* Xiaoli Zou; E-mail: zouxl1990@126.com
5 *Xinahua Hou; E-mail: houxh@scnu.edu.cn*
Yanling Huang; E-mail: yanling3963@126.com
b Engineering Research Center of Materials & Technology for Electrochemical Energy Storage (Ministry of Education), Guangzhou 510006, China
10 ** Shejun Hu; E-mail: husj@scnu.edu.cn*
Qiang Ru; E-mail: rq7702@yeah.net
c University of Electronic Science and Technology,Zhongshan Institute, Zhongshan,528400, China
Yumei Gao; E-mail: yumeigao@163.com
15

References

1 D. C. R. Espinosa and J. A. S. Tenório, J. Power Sources, 2006, **157**, 600-604.

2 P. Gao, Y. Wang, Q. Zhang, Y. J. Chen, D. Bao, L. Q. Wang, Y. Z. Sun, G. B. Li and M. L. Zhang, J. Mater. Chem., 2012, **22**, 13922.

3 T. V. Hoogerstraete and K. Binnemans, Green Chem., 2014, **16**, 1594.

4 Y. F. Liu, H. G. Pan, M. X. Gao and Q. D. Wang, J. Mater. Chem., 2011, **21**, 4743.

5 M. Li, X. H. Hou, Y. J. Sha, J. Wang, S. J. Hu, X. Liu, Z. P. Shao, J. Power Sources, 2014, **248**, 721-728.

6 Y. Chen, S. Zeng, J. F. Qian, Y. D. Wang, Y. L. Cao, H. X. Yang and X. P. Ai, ACS Appl. Mater. Interfaces, 2014, **6**, 3508-3512.

7 M. Zhang, X. H. Hou, J. Wang, M. Li, S. J. Hu, Z. P. Shao and X. Liu, J. Alloy Compd., 2014, **588**, 206-211.

8 J. Li, Q. Ru, S. J. Hu, D. W. Sun, B. B. Zhang and X. H. Hou, Electrochim. Acta, 2013, **113**, 505-513.

9 B. B. Zhang, C. Y. Wang, Q. Ru, S. J. Hu, D. W. Sun, X. Song and J. Li, J. Alloy Compd., 2013, **581**, 1-5.

10 K. Song, D. H. Seo, M. R. Jo, Y. I. Kim, K. Kang and Y. M. Kang, J. Phys. Chem. Lett., 2014, **5**, 1368-1373.

11 L. Cheng, J. Yan, G. N. Zhu, J. Y. Luo, C. X. Wang and Y. Y. Xia, J. Mater. Chem., 2010, **20**, 595-602.

12 L. M. Yao, X. H. Hou, S. J. Hu, J. Wang, M. Li, C. Su, M. O. Tade, Z. P. Shao, X. Liu, J. Power Sources, 2014, **258**, 305-313.

13 X. Song, Q. Ru, B. B Zhang, S. J Hu, B. N. An, J. Alloy. Compd., 2014, **585**, 518-522.

14 L. M. Yao, X. H. Hou, S. J. Hu, X. Q. Tang, X. Liu and Q. Ru, J. Alloy. Compd., 2014, **585**, 398-403.

15 H. M. Cheng, F. M. Wang, J. P. Chu, R. Santhanam, J. Rick and S. C. Lo, J. Phys. Chem., 2012, **116**, 7629-7637.

16 Y. S. Mizuno, N. Zettsu, K. Yubuta, T. Sakaguchi, T. Saito, H. Wagata, S. Oishi and K. Teshima. Cryst. Growth Des., 2014, **14**, 1882-1887.

17 J. J. Wang and X. L. Sun, Energy Environ. Sci., 2012, **5**, 5163.

18 R. G Mei, X. R. Song, Y. F. Yang, Z. G. An and J. J. Zhang, RSC Adv., 2014, **4**, 5746.

19 D. W. Han, W. H. Ryu, W. K. Kim, J. Y. Eom and H. S. Kwon, J. Phys. Chem., 2013, **117**, 4913-4919.

20 C. Lai, W. Y. Ye, H. Y. Liu and W. J. Wang, Ionics, 2009, **15**, 389-392.

21 M. Gao, F. Lian, H. Q. Liu, C. J. Tian, L. L. Ma and W. Y. Yang, Electrochim Acta, 2013, **95**, 87-94.

22 J.M. Zheng, X.B. Wu and Y. Yang, Electrochim. Acta, 2011, **56**, 3071-3078.

23 K. J. Rosina, M. Jiang, D. L. Zeng, E. Salager, A. S. Best and C. P. Grey, J. Mater. Chem., 2012, **22**, 20602.

24 X. H. Zhang, D. Luo, G. S. Li, J. Zheng, C. Yu, X. F. Guan, C. C. Fu, X. D. Huang and L. P. Li, J. Mater. Chem. A, 2013, **1**, 9721.

25 H. Koga, L. Croguennec, M. Ménétrier, P. Mannessiez, F. Weill, C. Delmas and S. Belin. J. Phys, Chem., 2014, **118**, 5700-5709.

26 H. J. Yu and H. S. Zhou, J. Phys. Chem. Lett., 2013, **4**, 1268-1280.

27 S. J. Shi, J.P. Tu, Y. Y. Tang, Y. X. Yu, Y. Q. Zhang and X. L. Wang, J. Power Sources, 2013, **221**, 300-307.

28 L. J. Zhang, B. Wu, N. Li, D. B. Mu, C. Z. Zhang, F. Wu, J. Power Sources, 2013, **240**, 644-652.

29 A. Boulineau, L. Simonin, J. F. Colin, C. Bourbon and S. Patoux, Nano Lett., 2013, **13**, 3857-3863.

30 J. M. Zheng, M. Gu, J. Xiao, P. J. Zuo, C. M. Wang and J. G. Zhang, Nano Lett., 2013, **13**, 3824-3830.

31 W. W. Liu, G. Q Fang, B. B. Xia, H. D. Sun, S. Kaneko and D. C. Li, RSC Adv., 2013, **3**, 15630.

32 Y. Cho, P. Oh, and J. Cho, Nano Lett., 2013, **13**, 1145-1152.

33 S. J. Shi, J.P. Tu, Y. J. Zhang, Y. D. Zhang, X. Y. Zhao, X. L. Wang and C. D. Gu, Electrochim. Acta, 2013, **108**, 441-448.

34 B. H. Song, M. O. Lai, Z. W. Liu, H. W Liu and L. Lu, J. Mater. Chem. A, 2013, **1**, 9954.

35 Q. Q. Qiao, H. Z. Zhang, G. R. Li, S. H. Ye, C. W. Wang and X. P. Gao, J. Mater. Chem. A, 2013, **1**, 5262

36 H. Z. Zhang, Q. Q. Qiao, G. R. Li, S. H. Ye and X. P. Gao, J. Mater. Chem., 2012, **22**, 13104.

37 Z. Y. Zhang, Y. Q. Lai, Z. A. Zhang, K. Zhang and J. Li, Electrochim. Acta, 2014, **129**, 55-61.

38 S. Y. Yang, G. Huang, S. J. Hu, X. H. Hou, Y. Y. Huang, M. Y and G. T Lei, Mater. Lett., 2014, **118**, 8-11.

39 H. J. Kim, H. G. Jung, B. Scrosati and Y. K. Sun, J. Power Sources, 2012, **203**, 115-120.

40 C. S. Johnson, N. C. Li, C. Lefief, J. T. Vaughey and M. M. Thackeray, Chem. Mater. 2008, **20**, 6095-6106.

41 F. Wu, Z. Wang, Y. F Su, N. Yana, L. Y. Bao and S. Chen, J. Power Sources, 2014, **247**, 20-25.

42 Z. R. Chang, D. M. Dai, H. W. Tang, X. Yu, X. Z. Yuan and H. J. Wang, Electrochim. Acta, 2010, **55**, 5506–5510.

43 P. Lanz, C. Villevieille, P. Novák. Electrochim Acta, 2014, **130**, 206-212.

44 G. Singh, W. C. West, J. Soler and R. S. Katiyar, J. Power Sources, 2012, **218**, 34-38.

45 J. Y. Baek, H. W. Ha, I. Y. Kim and S. J. Hwang, J. Phys. Chem., 2009, **113**, 17392-17398.

46 M. Gu, A. Genc, I. Belharouak, D. P. Wang, K. Amine, S. Thevuthasan, D. R. Baer, J. G. Zhang, N. D. Browning, J. Liu and C. M. Wang, Chem. Mater., 2013, **25**, 2319-2326.

47 M. Gu, I. Belharouak, J. M. Zheng, H. M. Wu, J. Xiao, A. Genc, K. Amine, S. Thevuthasan, D. R. Baer, J. G. Zhang, N. D. Browning, J. Liu and C. M. Wang, ACS Nano., 2013, **7**, 760-767.

48 L. Li, X. X. Zhang, R. J. Chen, T. L. Zhao, J.Lu, F. Wu and K. Amine, J. Power Sources, 2014, **249**, 28-34.

49 O. Toprakci, H. Toprakci, Y. Li, L. W. Ji, L. G. Xue, H. Lee, S. Zhang and X. W. Zhang, J. Power Sources, 2013, **241**, 522-528.

50 J. Wang, B. Qiu, H. L. Cao, Y. G. Xia and Z. P. Liu, J. Power Sources, 2012, **218**, 128-133.

Table of Contents Entry

Surfactant CTAB-assisted $Li_{1.13}[Ni_{0.233}Mn_{0.534}Co_{0.233}]_{0.87}O_2$ composite present a stable mixed structure, which can effectively alleviate the layered/spinel structure change during the cycling and ensures high stable specific capacity (247.5 mAh g^{-1}).